CCS CHINESE CHEMICAL SOCIETY   PEKING UNIVERSITY   ROYAL SOCIETY OF CHEMISTRY

RESEARCH ARTICLE

Check for updates

Eu³⁺-MOF fluorescence sensor based on a dual-ligand strategy for visualised detection of an anthrax biomarker 2,6-pyridine dicarboxylic acid†

Runnan Wang,[a,b] Hao Zhang,[b] Jing Sun*[a] and Zhongmin Su ⓘ *[a]

Bacillus anthracis is an extremely dangerous bacterium that causes high morbidity and mortality. Developing a simple and effective sensor to detect its unique biomarker 2,6-pyridine dicarboxylic acid (DPA) is urgently required to prevent anthrax infection. In this work, a ratiometric fluorescence sensor based on lanthanide–metal–organic frameworks (MOFs) was developed for the sensitive and selective recognition of DPA. Eu-MOF was successfully synthesised by Eu³⁺, 2,5-thiophenedicarboxylic acid, 2-aminoterephthalic acid, and dimethylformamide (DMF) through a simple solvothermal method. The rationally designed Eu-MOF not only exhibited outstanding sensitivity, strong stability and excellent anti-interference ability for DPA detection but also realised an obvious naked-eye colour change from red to blue with the increasing DPA concentration under UV light. Moreover, a possible detection mechanism involving hydrogen bonding, coordination and photoinduced electron transfer between the Eu-MOF and DPA was proposed. More importantly, the application of Eu-MOF probes in fetal calf serum and tap water also obtained satisfactory results, and the Eu-MOF probes were immobolised onto polyvinyl alcohol membrane, achieving a portable and convenient approach to monitoring DPA.

1. Introduction

Anthrax is a severe infectious zoonosis disease caused by *Bacillus anthracis*.[1,2] Inhalation of *Bacillus anthracis* spores exceeding 104 CFU mL⁻¹ is fatal within 24 hours without proper medical treatments.[3] *Bacillus anthracis* spores transform into active pathogenic *Bacillus anthracis* when heated and broken down. The pathogens can germinate and grow even under extreme conditions accompanied by the release of 2,6-dipicolinic acid (DPA).[4,5] DPA is an important component and a major biomarker for bacillus anthrax spores, which accounts for 5–15% of their dry weight.[6–8] Therefore, accurate measurement of DPA is of the utmost importance to prevent anthrax infection and protect public health.[9]

At present, many methods have been investigated for detecting DPA, such as high-performance liquid chromatography,[10] polymerase chain reaction,[11] surface enhanced Raman spectroscopy,[12] immunoassays,[13] and fluorescence spectroscopy.[14,15] Fluorescent sensors have demonstrated application potentials because of their simple operation, high sensitivity, portability, high efficiency, and low cost. Among many photoluminescent sensors, metal–organic frameworks (MOFs), especially lanthanide-MOFs (Ln-MOFs), have displayed unique optical properties, including long fluorescent lifetimes, sharp emission, high colour purity, and large Stokes shifts.[16–18] More importantly, the highly coordinated lanthanide centre ions in Ln-MOFs enable accurate recognition of DPA because they have a strong binding affinity for DPA and provide coordination sites to form stable complexes.[19]

Ln-MOFs with dual-luminescence centres can achieve self-calibration and reduce the influence of external environmental disturbance, thereby showing higher sensing performance than Ln-MOFs with a single emission centre.[20] In addition, dual-emission centres can construct ratio-metric fluorescent detection, and the ratio of the intensity at two different wavelengths exhibits a unique colour change under UV.[21] Dual-lanthanide ions (especially Eu³⁺ and Tb³⁺) in Ln-MOFs and emissive guest-doped Ln-MOFs have been applied to detect DPA. However, the guest dopants are unstable and may leach from the framework. The dual lanthanide ions in Ln-MOFs may lack uniformity, and the analytes may have the same effects for both lanthanide ions and reduce the anti-inter-

[a]*School of Chemistry and Environmental Engineering, Changchun University of Science and Technology, Jilin Provincial Science and Technology Innovation Center of Optical Materials and Chemistry, Jilin Provincial International Joint Research Center of Photo functional Materials and Chemistry, Changchun, 130022, PR China. E-mail: sj-cust@126.com, zmsu@nenu.edu.cn*

[b]*Department of Analytical Chemistry, Jilin Institute of chemical Technology, the Key Laboratory of Fine Chemicals of Jilin Province, Jilin, 132022, PR China*

This journal is © the Partner Organisations 2024

Inorg. Chem. Front., 2024, **11**, 269–277 | 269

ference ability of the Ln-MOFs testing system.[22] To overcome the above limitations, efforts have been made to choose suitable organic ligands to offer another luminescent centre to realise dual emissions. However, dual-ligand Ln-MOFs based on single Ln^{3+} are seldom reported.

Herein, we synthesised a single-Ln^{3+}-based dual-ligand Ln-MOFs fluorescence probe for DPA sensing by a simple self-assembly method. Based on our previous work,[23] 2-aminoterephthalic acid (NH_2-BDC) and 2,5-thiophenedicarboxylic acid (H_2TDA) were selected as organic ligands, and Eu^{3+} was employed as the single Ln^{3+} luminescent centre. Eu-MOF with a new crystal structure was prepared under solvothermal conditions and exhibited excellent performance for DPA detection in ethyl alcohol solutions, real fetal calf serum, and tap water. Using the ratio between the characteristic fluorescence emission of Eu^{3+} and H_2TDA ligand, ratio-metric and visual fluorescent probe was constructed. After Eu-MOF reacted with DPA, an obvious colour change from red to blue fluorescence was observed due to the hydrogen bonding and coordination effects. Eu-MOF was further immobilised in membranes and exhibited an outstanding response sensitivity and naked-eye colour change. To our knowledge, it is the first dual-ligand Ln-MOFs based on a single Ln^{3+} centre for portable DPA detection, which may pave the way for constructing simple, efficient, and convenient fluorescence sensors.

2. Experimental

2.1. Synthesis of Eu-MOF

NH_2-BDC (1 mL, 0.05 M), $Eu(NO_3)_3 \cdot 6H_2O$ (1 mL, 0.1 M), H_2TDA (1 mL, 0.1 M), and dimethylformamide (DMF, 2 mL) were successively added into a beaker and sonicated for 30 min. Then, the mixture was transferred into a 10 mL Pyrex vial and heated in an isothermal oven at 120 °C for 72 h, subsequently cooled to 25 °C at 10 °C h^{-1}. The colourless crystals were collected after centrifugation and washed with fresh DMF and deionised water repeatedly. The yield of Eu-MOF crystals was 77.2% based on $Eu(NO_3)_3 \cdot 6H_2O$.

2.2. Fluorescence sensing of DPA

First, the Eu-MOF powder was uniformly dispersed into an ethyl alcohol solution (1 mg mL^{-1}) to prepare an Eu-MOF suspension. Subsequently, different concentrations of DPA solution (300 μL) were added into 2.7 mL of Eu-MOF ethyl alcohol solution, and the resulting mixture was shaken for 3 min at room temperature to allow a complete reaction. Then, the fluorescence spectra were recorded immediately with an excitation wavelength of 330 nm. Subsequently, several substances with similar structures to DPA were added using the same method for selectivity and anti-interference experiments.

2.3. Preparation of Eu-MOF test membrane for DPA assay

The preparation method is similar to our group's previous work.[24] Polyvinyl alcohol (PVA 1788, 5 g) was placed in 20 mL of deionised water and sonicated for 30 min. After soaking

overnight, the PVA was thoroughly moistened. Then, the above mixture was stirred and heated at 90 °C in a water bath for 4 h to allow PVA to dissolve completely. Next, 5 g of Eu-MOF was added to the cooled PVA solution and stirred vigorously with a glass stick. The mixture was then coated on a microscope slide and dried at 60 °C overnight. Finally, the PVA@Eu-MOF membrane was cut into strips of 1 cm × 2 cm or a circle with a diameter of 1 cm.
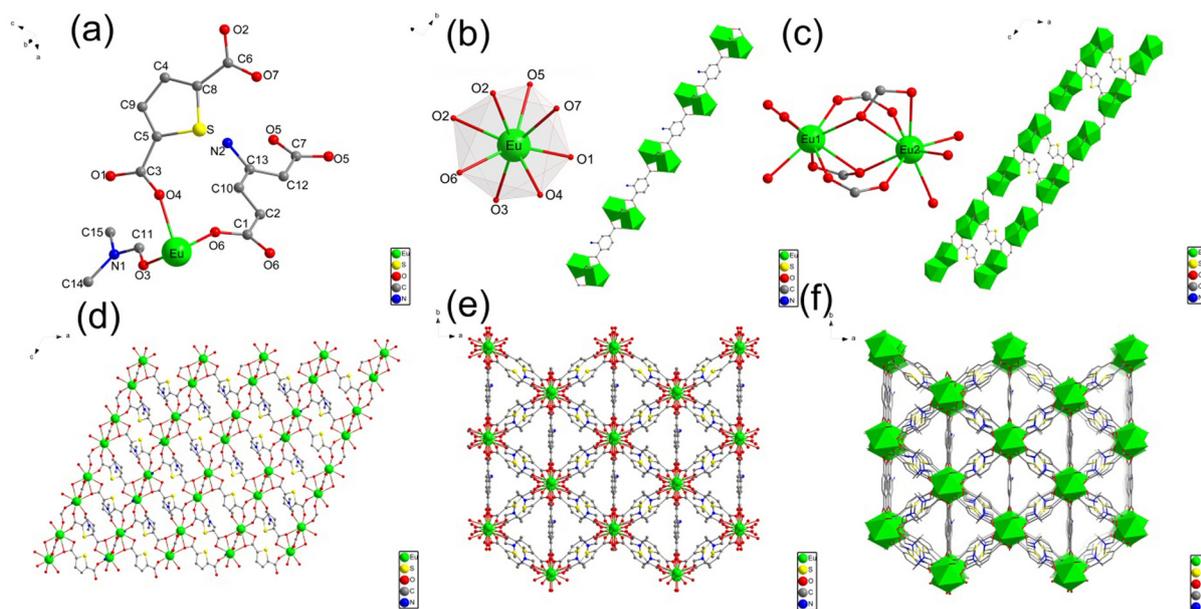
3. Results and discussion

3.1. Structural analysis

The single-crystal X-ray diffraction (XRD) analysis shows that Eu-MOF crystallises in a monoclinic $C2/c$ space group and possesses a three-dimensional (3D) framework. The structure of Eu-MOF is shown in Fig. 1. The asymmetric unit of Eu-MOF includes one crystallographically independent Eu^{3+} ion, one TDA ligand, half NH_2-BDC ligand and a free DMF molecule (Fig. 1a). The centre Eu^{3+} atom is coordinated to eight oxygen ligands and forms a dodecahedron structure (Fig. 1b), wherein two of them (O5 and O6) are from 1.5 BDC-NH_2 ligands, five of them (O1, O2, O2, O4, and O7) are provided by carboxyl oxygen atoms from four TDA ligands, and the other one is coordinated with one free DMF molecule (O3). In Eu-MOF, two adjacent Eu^{3+} ion centres are bridged by surrounding two carboxylate groups from two TDA ligands (O2, O7), and one carboxylate group from NH_2-BDC (O5, O6) to form a $Eu_2(COO)_3$ secondary building units (Fig. 1c). These $[Eu_2(COO)_3]$ subunits interconnect with the organic linker (NH_2-BDC) to generate an infinitely extended one-dimensional (1D) chain structure along the b-axis. The TDA ligand contains two carboxylate groups that connect three $[Eu_2(COO)_3]$ subunits (Fig. 1c), $i.e.$, the carboxylate (O7–C6–O2) links two Eu(III) centres in one $[Eu_2(COO)_3]$ subunit, and the other carboxylate (O1–C3–O4) joins two Eu(III) in two separate $[Eu_2(COO)_3]$ subunits. Thus, the TDA ligand participates in the coordination to form two-dimensional (2D) lattice-like layers along the ab-plane (Fig. 1d) and the adjacent layers connected by TDA repeat parallelly and stack to develop a 3D framework structure (Fig. 1f). Details of the single crystals are listed in Tables S1, S2 and S3, and the CCDC number is 2293720.†

3.2. Characterisation of Eu-MOF

Powder X-ray diffraction (PXRD) analysis was used to analyse the crystal structure of Eu-MOF (Fig. 2a). The PXRD pattern of Eu-MOF shows sharp diffraction peaks, which are almost identical to the simulated pattern acquired by the single crystal structure data of Eu-MOF, suggesting the high purity of the Eu-MOF phase.[25]

The Fourier-transform infrared spectroscopy (FT-IR) spectra of Eu-MOF, NH_2-BDC, and TDA are shown in Fig. 2b. The characteristic peaks at 3506 cm^{-1}, 3442 cm^{-1}, and 3455 cm^{-1} in NH_2-BDC, TDA and Eu-MOF are related to the O–H bonds.[26] The peaks at 3393 cm^{-1} and 1623 cm^{-1} belong to the stretching absorption and bending vibration of –NH_2 in NH_2-BDC,

270 | *Inorg. Chem. Front.*, 2024, **11**, 269–277

This journal is © the Partner Organisations 2024

Fig. 1 Crystal structures of Eu-MOF. (a) Asymmetrical unit of Eu-MOF. (b) Coordination environment of Eu^{3+} and 1D structure in the *b*-axis of Eu-MOF. (c) The $[Eu_2(COO)_3]$ dinuclear cluster structural unit and 1D in the *c*-axis of Eu-MOF. (d) 2D structure of Eu-MOF from ac plane. (e) 2D structure of Eu-MOF from ab plane. (f) 3D framework of Eu-MOF.
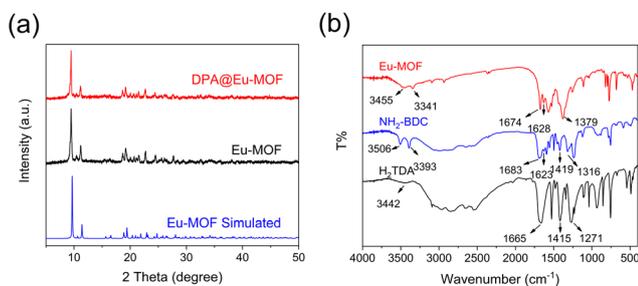
Fig. 2 (a) PXRD patterns of Eu-MOF, simulated Eu-MOF, and DPA@Eu-MOF. (b) FT-IR spectra of Eu-MOF, NH_2-BDC and H_2TDA.

respectively.[27–29] The absorption bands at 1665 cm^{-1}, 1415 cm^{-1} in TDA and 1683 cm^{-1}, 1419 cm^{-1} in NH_2-BDC are related to the asymmetric and symmetric stretching vibration of C=O,[30] respectively. These characteristic peaks shift to 1674 cm^{-1} and 1379 cm^{-1} in Eu-MOF, illustrating that the –COOH groups in the ligands coordinate with Eu^{3+}.[31] Besides, the bands observed at 1217 cm^{-1} and 1316 cm^{-1} disappear in Eu-MOF, also demonstrating the coordination with Eu^{3+}.[32] All the above observations confirm the successful synthesis of Eu-MOF.

The thermal stability of Eu-MOF was determined by the thermogravimetric analysis (TGA) under N_2 atmosphere (Fig. S1a†). The TGA curve of Eu-MOF has three main weight losses during the course of the weight lose. The earliest weight loss before 100 °C represents the removal of water molecules in Eu-MOF. The second weight loss (14.41%, calcd: 14.91%) occurs from 260 °C to 345 °C, which may correspond to the release of DMF solvent molecule. Further, a sharp weight loss

is observed around 470 °C, signifying the decomposition of the Eu-MOF framework skeleton. The TGA results verify the high thermal stability of Eu-MOF, which is favourable for its practical application.

The solid-state luminescence spectra of Eu-MOF are presented in Fig. S1b.† Upon excitation at 330 nm, the emission spectra of Eu-MOF exhibit three characteristic peaks at 593, 619, and 654 nm, ascribed to the $^5D_0 \rightarrow {}^7F_J$ ($J = 1, 2,$ and 3) transitions of Eu^{3+} ions,[33,34] respectively. Under UV irradiation, the luminescent colour of Eu-MOF appears red. The solid-state luminescence spectrum of Eu-TDA was also carried out to understand the influence of TDA and NH_2-BDC ligands on the fluorescence properties of Eu-MOF. The Eu-TDA was synthesised using a similar method to obtain Eu-MOF in the absence of NH_2-BDC. Eu-TDA also displays strong Eu^{3+} characteristic emission peaks, indicating that the TDA ligand can be a suitable "antenna" for the emission process of Eu^{3+} in Eu-TDA and Eu-MOF. Our previous work also supports this viewpoint.[23] The energy gap (ΔE) between Eu^{3+} and triplet-state energy (T1) of BDC-NH_2 is lower than 2500 cm^{-1}, which is the minimum energy range for effective sensitisation.[35,36] Whereas, the ΔE between Eu^{3+} and T1 of TDA matches the optimal energy level required for ligand-to-metal charge transfer (LMCT) process. According to the Latva's rules,[37] TDA ligand is more efficient than NH_2-BDC for the fluorescent luminescence process of Eu-MOF.

3.3. Sensing property for DPA

First, detection medium was selected by immersing the Eu-MOF in different organic solvents, including ethyl alcohol (EtOH), methyl alcohol (MeOH), *N,N*-Dimethylformamide

This journal is © the Partner Organisations 2024

Inorg. Chem. Front., 2024, **11**, 269–277 | **271**

(DMF), acetonitrile (ACN), isopropanol (IPA), benzene (PhH), methylbenzene (PhMe), dichlorotoluene (2,4-DCT), *N*,*N*-Dimethylaniline (DMA), ethyl acetate (EA), and 1-Pentanol (PEN) (Fig. S2†). Ethanol solution shows the minimum intensity ratio of I_{434}/I_{619} and the strongest emission peak of Eu^{3+} ions. Therefore, ethyl alcohol was chosen as the detection medium. Furthermore, the fluorescence stability of Eu-MOF in ethanol–water (v : v = 9 : 1) solution was studied. Eu-MOF showed negligible changes of intensity after immersing in ethanol–water solution for 10 days (Fig. S3†). Stable intensity at a wide pH range (pH = 3–12) (Fig. S4†) also proved good fluorescence stability in the detection environment. Then, the effect of reaction time on the detection of DPA was researched. The fluorescence emission curves were recorded within different periods after the DPA aqueous solution was mixed with Eu-MOF ethanol suspension and shaken for 3 min. As shown in Fig. S5,† the intensity of the emission peak at 434 nm increases rapidly in the first 1 min. The ratio of I_{434}/I_{619} reaches equilibrium within 3 min, implying a fast response of Eu-MOF to DPA.

To research the sensitivity of Eu-MOF for DPA detection, DPA solutions of different concentrations (0 to 500 μM) were mixed with Eu-MOF, and the fluorescence spectra were recorded. As shown in Fig. 3a, the luminescence intensity at 434 nm increases gradually when the concentration of DPA increases from 0 to 500 μM, while the fluorescence intensity at 619 nm shows insignificant change. Fig. 3b shows the relationship between I_{434} and I_{619} with DPA concentration. The I_{434} increases by 10 times with the DPA concentration and is used as the identification signal in the sensing, and the unchanged I_{619} is used as the reference signal. Because the characteristic peak of NH_2-BDC ligand is observed in the spectrum, DPA detection experiments were also conducted using the separate NH_2-BDC ligand. As shown in Fig. S6a,† NH_2-BDC only shows a slight increase in the signal with the increasing DPA concen-

tration, and their corresponding CIE coordinates all are located in the blue area (Fig. S6b†). However, Eu-MOF shows a distinct emission colour change from red to blue (Fig. 3d), which can be observed with the naked eye. This is an advantage of the dual-ligand strategy for constructing Ln-MOF sensor. The relationship between the I_{434}/I_{619} of Eu-MOF and DPA concentration (0–500 μM) is shown in Fig. 3c. The linear equation is $Y = 1.33824 + 0.02949X$ (R^2 = 0.9973). The limit of detection (LOD) is calculated as 0.41 μM based on a 3σ/slope, which is much lower than the human infection dose of bacterial endospores (60 μM).[38] In comparison with previously reported MOF probe, Eu-MOF has higher or equivalent sensitivity for DPA detection (Table S4†).
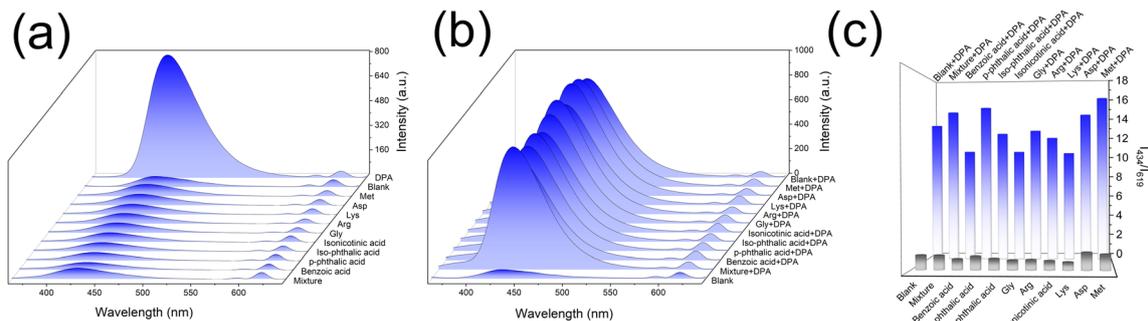
To investigate the selectivity of the proposed DPA sensing platform, multiple organic molecules with similar structures to DPA and amino acids were selected for the selectivity test, including Benzoic acid, *p*-phthalic acid, Iso-phthalic Acid, Isonicotinic acid, Gly, Arg, Lys, Asp, Met and the mixture of these compounds. As presented in Fig. 4a, these compounds have no obvious changes to the luminescence of Eu-MOF, while DPA exhibited remarkable enhancement at 434 nm. Considering the complexity of the test environment, the interference study were further conducted (Fig. 4b). The Eu-MOF emitted similar fluorescence upon exposure to DPA despite coexists with various interfering substances. Therefore, Eu-MOF has high selectivity and anti-interference ability, revealing enormous potential in the rapid and accurate detection of anthrax biomarkers in complex environments.

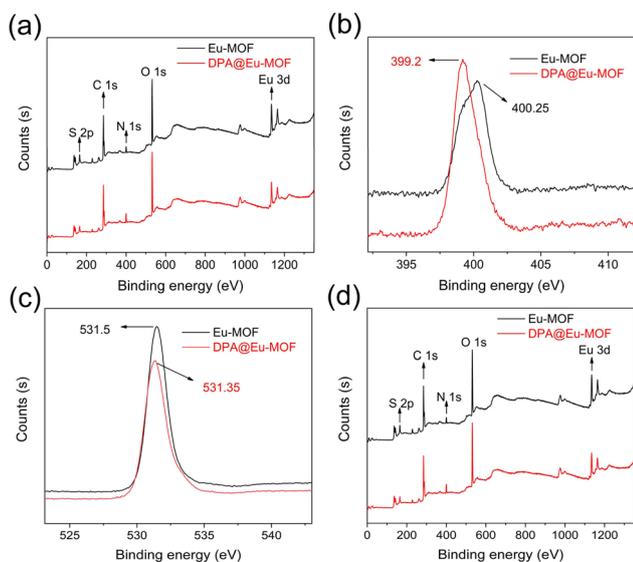### 3.4. Mechanism for Eu^{3+}-MOF detection DPA

To understand the plausible detection mechanism of Eu-MOF, PXRD, UV–vis, FT-IR and X-ray photoelectron spectroscopy (XPS) were conducted on Eu-MOF after DPA sensing (DPA@Eu-MOF). First, as recorded in Fig. 2a, the PXRD pattern of DPA@Eu-MOF maintains a high degree of consistency and structural integrity, ruling out the possibility of crystal collapse and disintegration. Next, the fluorescence emission spectrum of DPA ligand, Eu-MOF and DPA@Eu-MOF is compared (Fig. S7a†). It can be obtained that DPA has no fluorescence emission at 434 nm. Then, it can be seen by the absorption spectra of DPA and Eu-MOF that there is basically no absorption peak around 330 nm (excitation wavelength) at the UV-vis absorption spectrum of DPA, and neither overlaps between DPA and Eu-MOF (Fig. S7b†), which illustrates the inexistence of internal filtering effect process and competitive energy absorption and between Eu-MOF and DPA.[39] Next, the FT-IR of DPA@Eu-MOF, Eu-MOF, and DPA are compared (Fig. S8a†). The stretching vibration of $-NH_2$ group at 3341 cm^{-1} in Eu-MOF shifts to 3347 cm^{-1} in DPA@Eu-MOF. Meanwhile, the O–H stretching vibrations at 3436 cm^{-1} in Eu-MOF and 3425 cm^{-1} in DPA shift to 3441 cm^{-1} in DPA@Eu-MOF. Considering the structure of the ligands, it is inferred that the $-NH_2$ in Eu-MOF forms N–H⋯O hydrogen bond with the carboxyl oxygen in DPA,[40–42] thereby enhancing the luminescence of the ligand. The interaction between Eu-MOF and DPA was further examined by XPS. As displayed in Fig. 5b, the binding
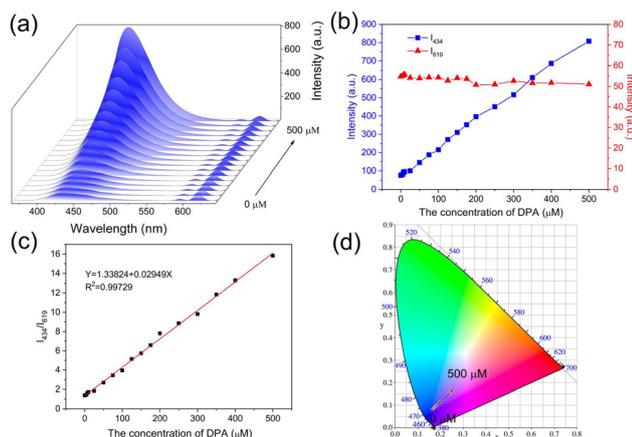
Fig. 3 (a) Fluorescence spectra of Eu-MOF with 0 to 500 μM DPA. (b) Relationship between luminescence intensity of 434 and 619 nm *versus* DPA concentration. (c) Standard curve of $\Delta(I_{434}/I_{621})$ *versus* DPA concentration. (d) CIE chromaticity diagram of Eu-MOF in the presence of 0 to 500 μM DPA.

272 | *Inorg. Chem. Front.*, 2024, **11**, 269–277

This journal is © the Partner Organisations 2024

Fig. 4 (a) Fluorescence spectra of Eu-MOF treated with amino acids and various organic molecules with similar structures to DPA. (b) Fluorescence spectra of Eu-MOF upon exposure to DPA with the coexistence of other organic components. (c) The corresponding fluorescence intensity ratio of I_{434}/I_{621}.
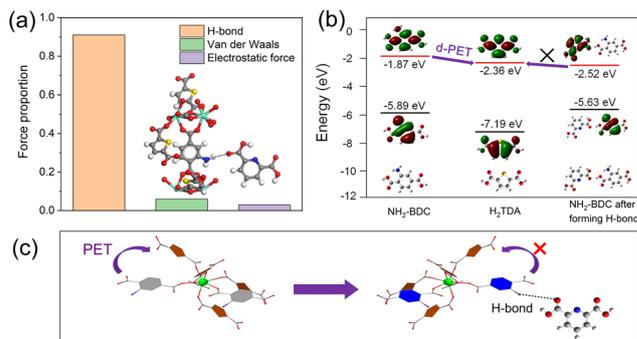

Fig. 5 XPS spectra of (a) survey scan, (b) N 1s, (c) O 1s, and (d) Eu 3d of Eu-MOF and DPA@Eu-MOF.

In order to verify the formation of N–H⋯O functional groups in DPA sensing process, interaction force between Eu-MOF and DPA are further studied through the density functional theory calculation. As shown in Fig. 6a. The adsorption energy generated by the effect of hydrogen bond, van der Waals and electrostatic force are −2.948, −0.194 and −0.097 eV, respectively, and the proportion 0.91, 0.06 and 0.03, respectively. The calculation results show that the hydrogen bond plays a dominant role between two molecules and it is facilitate to form hydrogen bonds between Eu-MOF and DPA.

Finally, the molecular orbitals of NH_2-BDC ligand, H_2TDA ligand are calculated. As showen in Fig. 6b, the lowest unoccupied molecular orbital (LUMO) of H_2TDA is −2.36 eV, which is lower than that of NH_2-BDC (−1.87 eV). Hence, the photo-induced electron transfer (fluorophore as the donor) (d-PET) process in Eu-MOF could occurred from NH_2-BDC to H_2TDA, leading to an extremely weak emission of NH_2-BDC in Eu-MOF. However, when Eu-MOF detected DPA, the hydrogen bonds of N–H⋯O between –COOH in DPA and –NH_2 in NH_2-BDC were formed. The LUMO energy level of new compounds decreased to −2.49 eV, which is lower than that of H_2TDA. Thereby, the d-PET process was prevented from the LUMO of

energy of N 1s shifts from 400.25 for Eu-MOF to 399.2 eV for DPA@Eu-MOF, suggesting that the density of the electron cloud around N changes because of the formation of N–H⋯O hydrogen bond.[43,44]

In addition, new absorption peaks ascribed to the C–N stretching vibrations in pyridine ring appear at 1076 and 1281 cm^{-1} on the FT-IR spectrum of DPA@Eu-MOF (Fig. S8b†), illustrating that DPA coordinates with Eu-MOF.[45,46] XPS spectra further verify the coordination between DPA and Eu-MOF. As presented in Fig. 5d, the two peaks at 1135.04 and 1164.68 eV in Eu-MOF shift to 1134.74 and 1164.56 eV, respectively, after interacting with DPA. The O 1s peak also shifts from 531.5 to 531.35 eV (Fig. 5c). The variations in the binding energy of O 1s and Eu 3d suggest that the coordination between Eu^{3+} and DPA can change the density of the electron cloud around the coordinated O atom in TDA or NH_2-BDC ligand.[47,48]

Fig. 6 (a) Force proportion of hydrogen bond, van der Waals and electrostatic force (inset: coordination configuration diagram of N–H⋯O hydrogen bond). (b) Calculated HOMO and LUMO energy levels of NH_2-BDC and H_2TDA. (c) Schematic illustration of the PET process of Eu-MOF sensing DPA.

This journal is © the Partner Organisations 2024

Inorg. Chem. Front., 2024, **11**, 269–277 | **273**

NH$_2$-BDC to that of H$_2$TDA and the fluorescence of NH$_2$-BDC was recovered at 434 nm (Fig. 6c).[49] Based on the above characterisations, it is concluded that the mechanism of Eu-MOF sensing is achieved through N–H⋯O hydrogen bonding, the coordination and photoinduced electron transfer process between Eu-MOF and DPA.

3.5. Applications in fetal calf serum and tap water samples

To investigate the practical feasibility of Eu-MOF, fetal calf serum and tap water were selected as sensing media for further investigation. The tap water was obtained from the laboratory of Jilin Institute of chemical Technology. All fetal calf serum samples were diluted 30-fold with ultrapure water and then filtered with filter paper to remove possible suspended particles before the experiment. Tap water was filtered by filter paper and tested directly before analysis with Eu-MOF. Different concentrations (20, 150 and 300 μM) of DPA solution were added to the prepared samples separately, and the luminescence was detected according to the same method mentioned above. As shown in Table 1, the recovery values of DPA from fetal calf serum and tap water are in the range of 97.0–101.6% and 97.5–103.4%, respectively. Further, the relative standard deviations (RSD, n = 3) of detection results are all under 3.4%. The satisfactory recovery and low RSD further prove the reliability and feasibility of the Eu-MOF for the detection of DPA in real environment samples.

3.6 Application of Eu-MOF@PVA test membrane detect DPA

Eu-MOF@PVA test membrane was used to detect DPA in ethyl alcohol. First, the properties of Eu-MOF@PVA membrane was characterised. In the PXRD pattern of Eu-MOF@PVA, the diffraction peaks are identical to those of experimental and simulated Eu-MOF, indicating that the En-MOF particles in Eu-MOF@PVA maintain high phase purity during the progress of film formation (Fig. S9a†).[50] In addition, the FT-IR spectra of Eu-MOF@PVA and Eu-MOF (Fig. S9b†) confirm that all chemical bonds remain unchanged during film preparation.

Next, scanning electron microscopy (SEM) and energy dispersive spectroscopy (EDS) were carried out to characterise the morphology of Eu-MOF@PVA. As shown in Fig. 7, Eu-MOF particles are uniformly distributed on the surface and cross-section of the membrane. EDS mapping shows that the contents of O, S, C, Eu, and N elements are 57.52%, 12.79%, 24.74%, 1.75%, and 3.20%, respectively (Fig. S10†), confirming
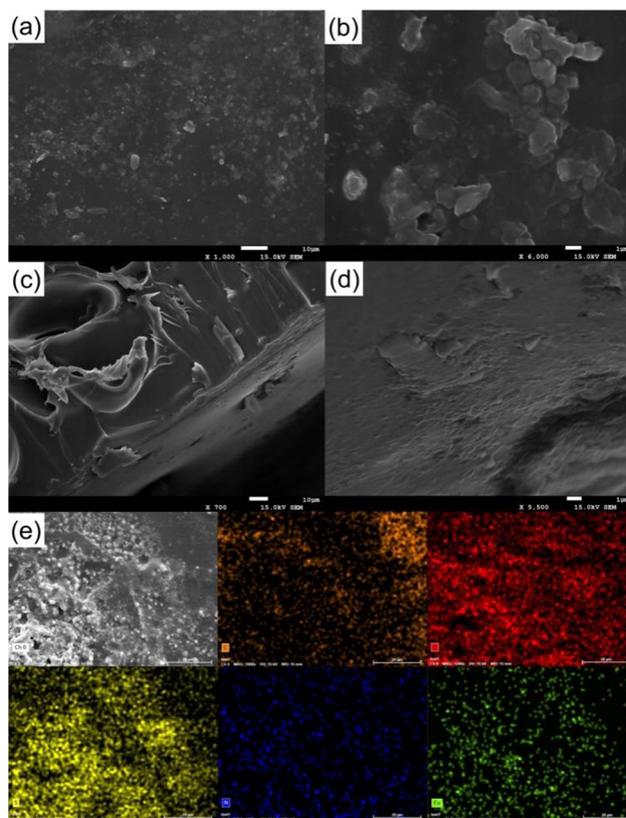

Fig. 7 (a and b) SEM images of Eu-MOF@PVA surface. (c and d) SEM image of Eu-MOF@PVA cross sections. (e) EDS mapping of Eu-MOF@PVA.

the integrity and homogeneity of the Eu-MOF@PVA. Furthermore, the Eu-MOF@PVA membrane can be bent and rolled without forming fractures on the surface (Fig. 8b), demonstrating its excellent mechanical properties. Under natural light, the Eu-MOF@PVA membrane has a smooth surface and high transmittance (Fig. 8a and c), which are suitable for further senor development. Under UV irradiation at 254 nm, red emission of Eu-MOF@PVA membrane was observed. When the membranes were immersed in solutions

Table 1 Determination of DPA in fetal calf serum and tap water with Eu-MOF (n = 3)

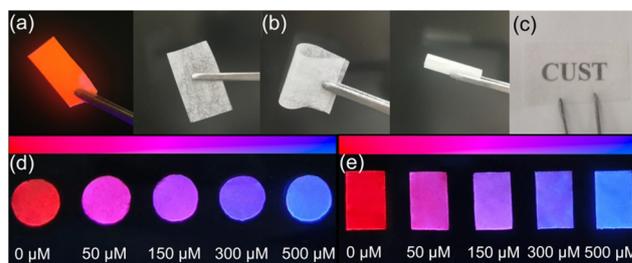| Samples	Added (μM)	Detected (μM)	Recovery (%)	RSD (%) (N = 6)
Fetal calf serum	20	19.4	97.0	3.4
	150	148.6	99.1	1.8
	300	304.9	101.6	0.3
Tap water	20	19.5	97.5	2.1
	150	155.1	103.4	1.5
	300	296.7	98.9	0.9

Fig. 8 (a) Eu-MOF@PVA under natural light and UV light. (b) Processability of Eu-MOF@PVA. (c) Transmittance of Eu-MOF@PVA. Colours of Eu-MOF@PVA test membranes under UV light irradiation with 0, 50, 150, 300, and 500 μM of DPA in (d) fetal calf serum and (e) tap water.

274 | *Inorg. Chem. Front.*, 2024, **11**, 269–277

This journal is © the Partner Organisations 2024

of fetal calf serum and tap water samples with 0, 50, 150, 300 and 500 μM of DPA, the fluorescent colour rapidly changed from red to blue gradually, which can be observed by the naked eye (Fig. 8d and e). The outstanding response sensitivity to DPA and the naked-eye visible colour change demonstrate that Eu-MOF@PVA membranes are promising sensitive, portable, and convenient sensors for DPA detection.

4. Conclusions

A dual-emission Eu-MOF with a new crystal structure of a monoclinic system and $C2/c$ space group was successfully prepared by NH_2-BDC, H_2TDA, $Eu(NO_3)_3 \cdot 6H_2O$, and DMF through a dual-ligand strategy. Eu-MOF demonstrates high phase purity, good stability, and excellent luminescent performance and can be used as a sensitive, efficient, selective, and convenient probe for DPA sensing. It also showed satisfactory practical applications to detect DPA in fetal bovine serum and tap water. Furthermore, the detection mechanism involving N–H⋯O hydrogen bonding, the coordination and photoinduced electron transfer process between Eu-MOF and DPA was proposed based on the PXRD, UV-vis, FT-IR, XPS and theoretical calculation results. More importantly, the successful exploit of Eu-MOF@PVA membranes provides a simple, convenient, and efficient platform for DPA detection.

Author contributions

The authors contributed equally to this work.

Conflicts of interest

There are no conflicts to declare.

Acknowledgements

References

1 X. Lin, H. Wu, S. Zeng, T. Peng, P. Zhang, X. Wan, Y. Lang, B. Zhang, Y. Jia, R. Shen and B. Yin, A self-designed device integrated with a Fermat spiral microfluidic chip for ratiometric and automated point-of-care testing of anthrax biomarker in real samples, *Biosens. Bioelectron.*, 2023, **230**, 115283.

2 D. Deng, J. Xu, T. Li, D. Tan, Y. Ji and R. Li, Dual-mode strategy for 2,6-dipicolinic acid detection based on the fluorescence property and peroxidase-like activity inhibition of Fe-MIL-88NH$_2$, *Spectrochim. Acta, Part A*, 2023, **291**, 122363.

3 K. Ai, B. Zhang and L. Lu, Europium-Based Fluorescence Nanoparticle Sensor for Rapid and Ultrasensitive Detection of an Anthrax Biomarker, *Angew. Chem.*, 2009, **121**, 310–314.

4 C. J. Carlson, W. M. Getz, K. L. Kausrud, C. A. Cizauskas, J. K. Blackburn, F. A. Bustos Carrillo, R. Colwell, W. R. Easterday, H. H. Ganz, P. L. Kamath, O. A. Kstad, W. C. Turner, A. Kolstø and N. C. Stenseth, Spores and soil from six sides: interdisciplinarity and the environmental biology of anthrax (Bacillus anthracis), *Biol. Rev.*, 2018, **93**, 1813–1831.

5 Y. Cao, X. Gong, L. Li, H. Li, X. Zhang, D. Guo, F. Wang and Q. Pan, Xylenol orange-modified CdTe quantum dots as a fluorescent/colorimetric dual-modal probe for anthrax biomarker based on competitive coordination, *Talanta*, 2023, **261**, 124664.

6 C. Huang, R. Ma, Y. Luo, G. Shi, J. Deng and T. Zhou, Stimulus Response of TPE-TS@Eu/GMP ICPs: Toward Colorimetric Sensing of an Anthrax Biomarker with Double Ratiometric Fluorescence and Its Coffee Ring Test Kit for Point-of-Use Application, *Anal. Chem.*, 2020, **92**, 12934–12942.

7 T. M. Koo, M. J. Ko, B. C. Park, M. S. Kim and Y. K. Kim, Fluorescent detection of dipicolinic acid as a biomarker in bacterial spores employing terbium ion-coordinated magnetite nanoparticles, *J. Hazard. Mater.*, 2021, **408**, 124870.

8 S. Pu, C. Shi, C. Lv, K. Xu, X. Hou and L. Wu, Tb^{3+}-Based Off-On Fluorescent Platform for Multicolor and Dosage-Sensitive Visualization of Bacterial Spore Marker, *Anal. Chem.*, 2023, **95**, 8137–8144.

9 S. Norouzi, K. Dashtian, F. Amourizi and R. Zare-Dorabei, Red-emissive carbon nanostructure-anchored molecularly imprinted Er-BTC MOF: a biosensor for visual anthrax monitoring, *Analyst*, 2023, **148**, 3379–3391.

10 K. Mawatari, M. Atsumi, F. Nakamura, M. Yasuda, T. Fukuuchi, N. Yamaoka, K. Kaneko, K. Nakagomi and N. Oku, Determination of Dipicolinic Acid in "Natto" by High-Performance Liquid Chromatography Coupled With Postcolumn Photoirradiation With Zinc Acetate, *Int. J. Tryptophan Res.*, 2019, **12**, 1178646919852120.

11 E. Bode, W. Hurtle and D. Norwood, Real-Time PCR Assay for a Unique Chromosomal Sequence of Bacillus anthracis, *J. Clin. Microbiol.*, 2004, **42**, 5825–5831.

12 X. Bai, Y. Zeng, X. Zhou, X. Wang, A. Shen and J. Hu, Environmentally Safe Mercury(II) Ions Aided Zero-Background and Ultrasensitive SERS Detection of Dipicolinic Acid, *Anal. Chem.*, 2017, **89**, 10335–10342.

13 D. King, V. Luna, A. Cannons, J. Cattani and P. Amuso, Performance assessment of three commercial assays for direct detection of Bacillus anthracis spores, *J. Clin. Microbiol.*, 2003, **41**, 3454–3455.

14 J. He, W. Lin, K. Wei, M. Yang, Z. Pu, Z. Tao and X. Xiao, Convenient cucurbit[8]uril-based supramolecular fluorescent probe for efficient detection of phenolic contaminants, *Dyes Pigm.*, 2023, **217**, 111403.

15 T. Gong, S. Yang, Z. Wang, M. Li, S. Zhang, J. Liu, L. Chen and J. Zhao, Dual-ligand-functionalized dodeca-nuclear

This journal is © the Partner Organisations 2024

Inorg. Chem. Front., 2024, **11**, 269–277 | **275**

lanthanide-tungsten-cluster incorporated selenotungstates and fluorescence detection of dipicolinic acid (an anthrax biomarker), *Inorg. Chem. Front.*, 2023, **10**, 2799–2810.

16 Y. Zhang, H. Lu and B. Yan, Determination of urinary N-acetylneuraminic acid for early diagnosis of lung cancer by a boric acid covalently functionalized lanthanide MOFs and its intelligent visual molecular robot application, *Sens. Actuators, B*, 2021, **349**, 130736.

17 W. Shi, S. Zhang, Y. Wang, Y. D. Xue and M. Chen, Preparation of dual-ligands Eu-MOF nanorods with dual fluorescence emissions for highly sensitive and selective ratiometric/visual fluorescence sensing phosphate, *Sens. Actuators, B*, 2022, **367**, 132008.

18 X. Yang, X. Lin, Y. Zhao, Y. S. Zhao and D. Yan, Lanthanide Metal-Organic Framework Microrods: Colored Optical Waveguides and Chiral Polarized Emission, *Angew. Chem.*, 2017, **129**, 7961–7965.

19 H. Li, X. He, M. Zhang, X. Li, R. Wang, Z. Xu and F. Li, Postsynthesis Strategy of Functional Zn-MOF Sensors for the Detection of ClO⁻ and DPA, *Inorg. Chem.*, 2021, **60**, 2590–2597.

20 W. Ma, X. Quan and B. Yan, A dual-emission Eu(III) functionalized multi-ligand MOFs for wide range pH sensing, *Dyes Pigm.*, 2022, **206**, 110648.

21 Y. Zhou, S. Zhao, W. Leng, X. Zhang, D. Liu, J. Zhang, Z. Sun, Y. Zhu, H. Zheng and C. Jiao, Dual-Functional Eu-Metal-Organic Framework with Ratiometric Fluorescent Broad-Spectrum Sensing of Benzophenone-like Ultraviolet Filters and High Proton Conduction, *Inorg. Chem.*, 2023, **62**, 12730–12740.

22 L. Yu, L. Feng, L. Xiong, S. Li, Q. Xu, X. Pan and Y. Xiao, Rational Design of Dual-Emission Lanthanide Metal-Organic Framework for Visual Alkaline Phosphatase Activity Assay, *ACS Appl. Mater. Interfaces*, 2021, **13**, 11646–11656.

23 R. Wang, H. Zhang, S. Wang, F. Meng, J. Sun, D. Lou and Z. Su, A ratiometric fluorescent probe based on a dual-ligand lanthanide metal-organic framework (MOF) for sensitive detection of aluminium and fluoride ions in river and tap water, *Inorg. Chem. Front.*, 2023, **10**, 1534–1542.

24 S. Wang, B. Sun, Z. Su, G. Hong, X. Li, Y. Liu, Q. Pan and J. Sun, Lanthanide-MOFs as multifunctional luminescent sensors, *Inorg. Chem. Front.*, 2022, **9**, 3259–3266.

25 S. Wu, J. Lin, J. Liu, W. Shi, G. Yang and P. Cheng, Rapid Detection of the Biomarkers for Carcinoid Tumors by a Water Stable Luminescent Lanthanide Metal-Organic Framework Sensor, *Adv. Funct. Mater.*, 2018, **28**, 1707169.

26 X. Zhao, H. Yang, W. Zhao, J. Wang and Q. Yang, A weakly luminescent Tb-MOF-based "turn-on" sensor for the highly selective and sensitive sensing of an anthrax biomarker, *Dalton Trans.*, 2021, **50**, 1300–1306.

27 H. Lin, J. Huang and L. Ding, Preparation of Carbon Dots with High-Fluorescence Quantum Yield and Their Application in Dopamine Fluorescence Probe and Cellular Imaging, *J. Nanomater.*, 2019, **2019**, 5037243.

28 Y. Jia, Z. Liu, X. Wang and B. Li, Synthesis of a novel hyperbranched polysiloxane with amidogen groups and the characteristics of a polymer alloy blend with bismaleimide resin, *High Perform. Polym.*, 2020, **32**, 12–20.

29 B. Lan, P. Li, Q. Yang and P. Gong, Dynamic self generation of hydrogen bonding and relaxation of polymer chain segment in stabilizing thermoplastic polyurethane microcellular foams, *Mater. Today Commun.*, 2020, **24**, 101056.

30 J. Zhao, J. Zhang, W. Yang, H. Wang, N. Zhang, Y. Fang and Q. Ke, Rational design of core-shell Ln-MOF hierarchitecture for ratiometric fluorescent sensing and bioimaging for phosphate or ATP, *Sens. Actuators, B*, 2023, **389**, 133907.

31 J. Xiao, M. Liu, F. Tian and Z. Liu, Stable Europium-based Metal-Organic Frameworks for Naked-eye Ultrasensitive Detecting Fluoroquinolones Antibiotics, *Inorg. Chem.*, 2021, **60**, 5282–5289.

32 M. Wu, Z. W. Jiang, P. Zhang, X. Gong and Y. Wang, Energy transfer-based ratiometric fluorescence sensing anthrax biomarkers in bimetallic lanthanide metal-organic frameworks, *Sens. Actuators, B*, 2023, **383**, 133596.

33 Y. Shi, X. Qu, Q. Lu, J. Zhao, Q. Ma, W. Sun, G. Ou Yang, W. Fu, X. Tao and D. Huang, Stable Lanthanide-Organic Frameworks: Crystal Structure, Photoluminescence, and Chemical Sensing of Vanillylmandelic Acid as a Biomarker of Pheochromocytoma, *Inorg. Chem.*, 2023, **62**, 6934–6947.

34 T. Tang, M. Liu, Z. Chen, X. Wang, C. Lai, L. Ding and C. Zeng, Highly sensitive luminescent lanthanide metal-organic framework sensor for L-kynurenine, *J. Rare Earths*, 2022, **40**, 415–420.

35 S. Dasari, S. Singh, Z. Abbas, S. Sivakumar and A. K. Patra, Luminescent lanthanide(III) complexes of DTPA-bis(amidophenyl-terpyridine) for bioimaging and phototherapeutic applications, *Spectrochim. Acta, Part A*, 2021, **256**, 119709.

36 Y. Hidalgorosa, J. Santoyoflores, M. A. Tretosuárez, E. Schott, D. Páezhernández and X. Zarate, Tuning the sensitization pathway T1→⁵D_J in Eu-based MOF through modification of the antenna ligand. A theoretical approach via multiconfigurational quantum calculations, *J. Lumin.*, 2023, **260**, 119896.

37 H. Li, M. Li, Y. Wang and W. Zhang, Luminescent Hybrid Materials Based on Laponite Clay, *Chem. – Eur. J.*, 2014, **20**, 10392–10396.

38 M. Qiu, K. Chen, Q. Liu, W. Miao, B. Liu and L. Xu, A ratiometric fluorescent sensor made of a terbium coordination polymer for the anthrax biomarker 2,6-dipicolinic acid with on-site detection assisted by a smartphone app, *CrystEngComm*, 2022, **24**, 132–142.

39 J. Xiu and G. Wang, Naphthalene-grafted MOF as a unique fluorescent sensor for "turn-off" detection for Fe³⁺ and "turn-on" detection for ClO₄⁻ in different solvents with high selectivity and sensitivity, *Sens. Actuators, B*, 2023, **374**, 132837.

40 Y. Wu, Y. Xu, D. Wang, Y. Zhao, S. Weng, D. Xu and J. Wu, FT-IR spectroscopic investigation on the interaction between nylon 66 and lithium salts, *J. Appl. Polym. Sci.*, 2004, **91**, 2869–2875.

41 J. Ma, Y. Shen, C. Shen, Y. Wen and W. Liu, Al-doping chitosan-Fe(III) hydrogel for the removal of fluoride from aqueous solutions, *Chem. Eng. J.*, 2014, **248**, 98–106.

42 A. Fatima, J. Bhadoria, S. K. Srivastava, I. Verma, N. Siddiqui and S. Javed, Exploration of experimental and theoretical properties of 5,5-dimethyl 3-amino-cyclohex-2-en-1-one (AMINE DIMEDONE) by DFT/TD-DFT with ethanol and DMSO as solvents and molecular docking studies, *J. Mol. Liq.*, 2021, **338**, 116551.

43 Z. Lin, L. Jin, Y. Liu and Y. Wang, Hydrogen bonding donor/acceptor active sites exposed on imide-functionalized carbon dots aid in enhancing arsenic adsorption performance, *Chem. Eng. J.*, 2023, **459**, 141540.

44 S. Liu, M. Liu, X. Li, Q. Xu, Y. Sun and G. Zeng, Construction of dense H-bond acceptors in the channels of covalent organic frameworks for proton conduction, *J. Mater. Chem. A*, 2023, **11**, 13965–13970.

45 F. M. Manhas, A. Fatima, I. Verma, N. Siddiqui, S. Muthu, H. S. AlSalem, S. Savita, M. Singh and S. Javed, Quantum computational, spectroscopic (FT-IR, NMR and UV-Vis) profiling, Hirshfeld surface, molecular docking and dynamics simulation studies on pyridine-2,6-dicarbonyl dichloride, *J. Mol. Struct.*, 2022, **1265**, 133374.

46 P. Huo, Z. Li, R. Yao, Y. Deng, C. Gong, D. Zhang, C. Fan and S. Pu, Dual-ligand lanthanide metal-organic framework for ratiometric fluorescence detection of the anthrax biomarker dipicolinic acid, *Spectrochim. Acta, Part A*, 2022, **282**, 121700.

47 X. Zhao, J. Wang, H. Hao, H. Yang, Q. Yang and W. Zhao, A water-stable europium-MOF sensor for the selective, sensitive ratiometric fluorescence detection of anthrax biomarker, *Microchem. J.*, 2021, **166**, 106253.

48 J. Dang, M. Li, W. Fang, Y. Wu, S. Xin, Y. Cao and H. Zhao, Amorphous amEu-NH$_2$BDC and amTb-NH$_2$BDC as ratio fluorescence probes for smartphone-integrated naked eye detection of bacillus anthracis biomarker, *Talanta*, 2024, **267**, 125164.

49 Y. Cui, D. Yue, Y. Huang, J. Zhang, Z. Wang, D. Yang and G. Qian, Photo-induced electron transfer in a metal-organic framework: a new approach towards a highly sensitive luminescent probe for Fe^{3+}, *Chem. Commun.*, 2019, **55**, 11231–11234.

50 H. Yu, Q. Liu, M. Fan, J. Sun, Z. Su, X. Li and X. Wang, Novel Eu-MOF-based mixed matrix membranes and 1D Eu-MOF-based ratiometric fluorescent sensor for the detection of metronidazole and PA in water, *Dyes Pigm.*, 2022, **197**, 109812.

This journal is © the Partner Organisations 2024

Inorg. Chem. Front., 2024, **11**, 269–277 | **277**